Multiscale modelling of thermoplastic woven fabric composites: From micromechanics to mesomechanics

J.I. Múgica[a,*], C.S. Lopes[a], F. Naya[a], M. Herráez[a], V. Martínez[a], C. González[a,b]

[a] *IMDEA Materials Institute, C/Eric Kandel, 2, 28906 Getafe, Madrid, Spain*
[b] *Department of Materials Science, Polytechnic University of Madrid, ETS de Ingenieros de Caminos, 28040 Madrid, Spain*

Abstract

The mechanical properties of woven composites can be predicted by using a multiscale modelling approach. The starting point to its application is the microscale (the level of fibres, matrix and interfaces), that allows the computation of the homogenised behaviour of the yarn. The aim of this work was to predict the yarn-level behaviour of a thermoplastic-based woven composite in order to allow the formulation of a representative constitutive model that can be used to predict ply properties at the mesoscale. To accomplish this purpose, an in-situ characterisation of the microconstituents was carried out. This served to generate inputs for three different representative volume element (RVE) models that allowed predicting the yarn longitudinal, transverse and shear responses. These mechanical characteristics allowed the determination of homogenised yarn constitutive behaviour which was found to be characterised by significant non-linearity until failure, specially in transverse and shear directions.

Keywords: woven composites, thermoplastics, multiscale modelling, computational micromechanics

1. Introduction

Advanced fibre-reinforced polymer (FRP) structures are manufactured using composite laminates, which in turn consist of composite layers stacked with different fibre orientations. Thus, within such architectures, various entities, such as fibre, layer or laminate/component, among others, are distinguished and each of them is associated to a specific length scale. These scales are characterised dimensionally by fibre diameter, layer thickness and laminate thickness, respectively, and are arranged in a hierarchical sequence (Fig. 1). When these advanced composite systems are subjected to mechanical loads, different

*Corresponding author at: IMDEA Materials Institute, C/Eric Kandel, 2, 28906 Getafe, Madrid, Spain.
Email address: joseba.mugica@imdea.org (J.I. Múgica)

deformation and failure mechanisms within the three length scales occur simultaneously. Faced with this fact, it is possible to design a bottom-up multiscale simulation scheme that takes advantage of the natural separation of the length scales between the aforementioned entities [1–3]. This method is based on virtually modelling the identifiable characteristic entities within a given scale and simulating their combined (or homogenised) response as if it were a single entity. Then, this response is taken to formulate a constitutive model that is assigned to the entity that it represents at a larger length scale. Such multiscale modelling strategy has proven to be a powerful tool that minimises experimental work, thus simplifying design tasks and greatly reducing associated costs. All this has been widely recognised in the context of the aeronautical industry, and others, where achieving maximum efficiency is a constant challenge [2, 3].

In the present study, the characteristic entities, identified within the microscale, are fibre, matrix and interface, from which it is intended to predict the response of a higher dimensional hierarchy entity, a yarn, which belongs to the scale of the ply (mesoscale). One way to obtain the corresponding homogenised response is through the use of so-called representative volume element (RVE) models. Quite a number of authors have demonstrated the accuracy of RVE models to predict stiffness, strength and fracture mechanisms of unidirectional (UD) FRPs under different loading conditions [4–8]. Moreover, RVE models have served to determine the complete failure surfaces of such materials [9–13]. By contrast, the volume of work that deals with the prediction of mechanical properties of woven composites based on a multiscale modelling approach is relatively small [14, 15].

This article constitutes the first part of a two-part work that addresses the study of the mechanical behaviour of a glass fibre-reinforced polypropylene (GFPP) woven composite on the basis of a bottom-up multiscale modelling strategy. The aim of this first part is to estimate the fundamental yarn properties of the above composite in order to formulate, in the second part of the work, a constitutive model that can be used to predict woven ply properties at the mesoscale. To accomplish this purpose, an in-situ microconstituent characterisation campaign was carried out. This served to feed three different representative volume element (RVE) models that allowed predicting tensile and compression behaviours, both longitudinal and transverse, as well as shear behaviour. Through them, the mechanical properties necessary to formulate a yarn constitutive model capable of reproducing its non-linear behaviour until failure were obtained.

[Figure 1 about here.]

2. Characterisation of microconstituents

The material studied herein is a GFPP twill 2/2 woven composite, which is commercialised under the trade name of Tepex® (dynalite 104-RG600(x)/47%) [16]. The properties necessary to model the matrix and interface behaviours were obtained by in-situ characterisation tests: nanoindentation for the matrix

and fibre push-in for the interface. To do so, samples were taken from a 1.5 mm thick 3-ply Tepex® laminate. These were set in resin leaving a free surface perpendicular to the yarns for in-situ characterisation tests. These tests were carried out with a Hysitron TI 950 TriboIndenter® nanoindenter. The experimental procedures are briefly described in this section (additional details are provided by Rodríguez *et al.* [17, 18]).

Taking advantage of the availability of the samples used to characterise the microconstituents, a microstructure study was carried out to determine the fibre diameter, $d_\mathrm{f} = 15.24 \pm 2.02$ µm (Gaussian distribution), and the local volume fraction, $V_\mathrm{f}^\mathrm{l} = 68\%$. As for the mechanical properties of the fibre, an elastic modulus, E^f, of 76 GPa and a Poisson's ratio, ν^f, of 0.22 were assumed; the strength properties were taken from experimental results available in the literature [19].

2.1. Matrix

Matrix nanoindentation was used to determine the elastic modulus, E^m, and the matrix compressive yield stress, $\sigma_{\mathrm{y}0}^\mathrm{c}$. This technique is based on the analysis of the mechanical response of the matrix when puncturing its surface. For this, it is usual to use an instrumented Berkovich tip. The use of such a tool causes a type of deformation in the material that leads to the appearance of either pile-up or the sink-in phenomena, depending on the material behaviour [18]. In this regard, it is essential to identify the phenomenon that results when a given nanoindentation test is performed to obtain matrix properties, as this allows to choose the appropriate procedure to obtain the properties. Oliver and Pharr established a methodology that provides satisfactory results when the material surrounding the tip sinks in [20]. Rodríguez *et al.* proposed a more complete and versatile alternative [18], validated for both sink-in and pile-up cases, which was used in the present research.

Based on the foregoing, five indentations at a strain rate of $0.1\,\mathrm{s}^{-1}$ and a limit penetration depth of 2 µm were made. Finally, the average values for the elastic modulus, E^m, and the matrix compressive yields stress, $\sigma_{\mathrm{y}0}^\mathrm{c}$, were obtained as 2.39 ± 0.18 GPa and 54.41 ± 2.66 MPa, respectively.

2.2. Fibre/matrix interface

The push-in test method was used to determine the fibre/matrix interface shear strength (ISS). By using an instrumented flat-tip nanoindenter, this technique basically consists in pushing a single fibre into the matrix until the occurrence of interface debonding [17]. This phenomenon is identified with the loss of linearity in the load-displacement curve recorded during the test. The push-in test only provides the value of the ISS in the longitudinal direction of the fibre, τ_l^0. The corresponding normal strength, σ_n^0, was assumed to be equal to $2/3\tau_\mathrm{l}^0$, based on the experimental results obtained by Ogihara and Koyanagi [21]. The ISS in the transverse direction of the fibre, τ_t^0, was considered equal to that of the longitudinal one ($\tau_\mathrm{t}^0 = \tau_\mathrm{l}^0 = \tau^0$). Such an assumption was considered reasonable since both matrix and fibres are isotropic materials.

In the present study, the nanoindenter was equipped with a 15 µm diameter flat tip. The indentations were made onto fibres whose diameter was slightly larger than that of the flat tip. Following the methodology proposed by Molina-Aldareguía *et al.* [22] to guarantee reproducibility, the tests were conducted on regions of highly packaged fibres following an hexagonal symmetry configuration, which was the most common format within the polymer matrix. A total of 10 push-in tests were performed. The average value of τ_1^0 was obtained as 22 MPa.

3. Computational micromechanics

Three different RVE models were developed to determine the fundamental yarn properties. Each of them was able to predict the mechanical response under specific solicitations. Thus, RVE–1 reproduced both transverse tension and compression behaviours, as well as in-plane shear response, while RVE–2 and RVE–3 modelled the longitudinal (fibre direction) tensile and compression behaviours, respectively. Table 1 collects the yarn properties to be determined with each of the RVE models. The model responses were numerically predicted based on an implicit integration scheme with Abaqus/Standard [23].

[Table 1 about here.]

3.1. Modelling features and constitutive equations

The matrix and fibres were meshed with 8-node linear brick elements (C3D8) and 6-node linear wedge elements (C3D6), respectively. In both cases, the elements were isoparametric and fully integrated. The interface debonding phenomenon, in the case of RVE–1, was simulated by means of 8-node brick cohesive elements (COH3D8), while in the cases of RVE–2 and RVE–3 cohesive surfaces were used. It was assumed that there was no imperfection or defect at the interface. Periodic boundary conditions (PBCs) were applied to the three pairs of opposite sides of all three models, thus ensuring the periodicity of the physical fields [24].

The matrix was modelled as an isotropic linear elastic-plastic material governed by the linear (original) Drucker-Prager yield criterion [25]. The so-called original model assumes the non-dependence on the third deviatoric stress invariant and an associated plastic flow [23]. Based on literature-available data [26], an internal friction angle of 13.71° was adopted. The corresponding yield surface evolved according to an exponential-type hardening function defined on the basis of compressive behaviour [23]. Fig. 2(a) shows the hardening function, formulated according to the mechanical properties obtained from the in-situ characterisation.

[Figure 2 about here.]

As for the fiber/matrix interface, the same constitutive law was used for both the cohesive elements (in RVE–1) and the cohesive surfaces (in RVE–2

and RVE–3). This model was governed by a linear elastic traction-separation law in which damage was assumed to be triggered by the following quadratic interaction stress criterion:

$$\left(\frac{\langle\sigma_{\mathrm{n}}\rangle}{\sigma_{\mathrm{n}}^{0}}\right)^{2}+\left(\frac{\tau_{\mathrm{l}}}{\tau_{\mathrm{l}}^{0}}\right)^{2}+\left(\frac{\tau_{\mathrm{t}}}{\tau_{\mathrm{t}}^{0}}\right)^{2}=1, \tag{1}$$

where $\langle\cdot\rangle$ stands for McCaulay brackets, defined as $\langle x\rangle=\max(0,x)$; σ_{n} is the normal stress; and τ_{l} and τ_{t} are the longitudinal and transverse stresses, respectively. The initial cohesive interaction response was assumed to be linear elastic characterised by a contact penalty stiffness, K. Once the damage began, the stiffness of the cohesive element was reduced based on a scalar damage parameter, D, whose value evolved from 0 (no damage) to 1 (totally damaged element). Fig. 2(b) represents the cohesive interaction response with respect to the effective displacement, δ_{m}, defined by Camanho and Dávila [27]. The damage evolution law was governed by the Benzeggagh-Kenane fracture criterion [28], which is written as:

$$G^{\mathrm{c}}=G_{\mathrm{n}}^{\mathrm{c}}+(-G_{\mathrm{n}}^{\mathrm{c}})\left(\frac{2G_{\mathrm{s}}}{G_{\mathrm{n}}+2G_{\mathrm{s}}}\right)^{\eta_{\mathrm{BK}}}, \tag{2}$$

where η_{BK} is the Benzeggagh-Kenane power exponent, $G_{\mathrm{n}}^{\mathrm{c}}$ and $G_{\mathrm{s}}^{\mathrm{c}}$ are the normal and shear fracture energies, respectively, and G_{n} and G_{s} are the reciprocal works under mixed mode fracture propagation.

The fibres were modelled as isotropic solids with linear-elastic behaviour up to failure. To properly capture longitudinal tensile failure, fracture planes were introduced perpendicular to the fibre direction by means of contacting surfaces governed by cohesive laws with stochastic failure parameters.

3.2. RVE–1: transverse tension/compression and shear

RVE–1 was a periodic quasi-2D model built on the basis of a spacial distribution of perfectly parallel circular fibres dispersed within the polymer matrix (see Fig. 3(a)). The cross-section height, h_0, represented by the RVE was 250 µm. Thus, the criterion of $h_0/d_{\mathrm{f}}\geq 8$, established by González *et al.* [4], which guarantees that the simulation results do not depend on h_0, was satisfied. The finite length, l_0, of the quasi-2D model was 1 µm, and it was discretised with a single plane of elements. The fibre spatial distribution was generated through the Random Sequential Adsorption (RSA) algorithm [24]. In order to obtain representative values of the properties, 5 realisations with random microestructures were made (average response is used for discussion).

[Figure 3 about here.]

3.3. RVE–2: longitudinal tension

RVE–2 was a full 3D model and, similarly to RVE–1, it was based on a extruded distribution of perfectly parallel circular fibres dispersed within the

matrix (see Fig. 3(b)). However, h_o was reduced to the minimum possible ($\approx 120\,\mu m$) so that the RVE size criterion [4] was satisfied while minimising the computational cost. In order to capture the longitudinal failure of the microstructure, in addition to considering the interface debonding mechanism through the use of cohesive surfaces, the fracture of the fibres was explicitly reproduced by modelling fracture planes perpendicular to the longitudinal fibre direction by means of cohesive surfaces (see Fig. 3(b)). Similar strategies were successfully used in previous works [12, 29, 30]. In the present case, the modelling strategy proposed by Naya [29] was adopted. The length, $l_0 = 600\,\mu m$, of the model was established based on the model of Curtin [31]. The strength of each fracture plane within fibres was randomly assigned according to a Weibull distribution [32]. The confined length to include the fracture planes as well as the separation distance between them depended on the Weibull strength and modulus parameters, $\sigma_0 = 3866\,MPa$ and $m = 5.5$, which were taken from literature-available data [19]. In order to obtain an approximate prediction of the average yarn longitudinal strength, it was essential to study the response of several different microstructures with their corresponding fibre longitudinal strength distributions. To this end, five different cases were analysed.

3.4. RVE–3: longitudinal compression

RVE–3 consisted of a periodic single fibre model (see Fig. 3(c)); an efficient approach previously validated by Naya *et al.* [33] and further exploited by Herráez *et al.* [34]. This model was conceived as a simplified version of the multifibre alternative and its use involves substantial computational savings while providing meaningful results. The compressive failure of the model is triggered by instability due to the presence of an imperfection that represents the initial fibre misalignment, ϕ_0. To consider this feature, the model is built by extruding the cross section of the representative volume along a sinusoidal path. The imperfection was intended to cause a type of failure that represented the fibre kinking phenomenon. The diameter of the fibre coincided with that of the mean value, d_f, and the cross section dimensions ($h_0 = w_0$) were imposed so that V_f^l was maintained. The length of the RVE was half the wavelength of the sinusoidal function used to represent de misalignment imperfection. With parametric analyses, RVE–3 was able to provide the longitudinal compressive strength, X^c as a function ϕ_0.

4. Results

In this section, the model-predicted response of the yarn to the proposed solicitations is presented. The analysis culminates with the characterisation of the yarn materialised by the determination of its mechanical properties. As an advance, Table 2 collects the characteristics of the predicted yarn behaviour obtained from the RVE models.

4.1. RVE–1: transverse tension/compression and shear

The response of the microstructure to the solicitations herein presented (transverse tension/compression and in-plane shear) resulted in all cases non-linear (see Fig. 4). This fact contrasts, considering specifically transverse load cases, with the corresponding response provided by composites based on thermoset matrices, such as epoxy ones [29, 33]. Thus, to characterise the responses obtained from the different load cases, Ramberg-Osgood equation was fitted for each of the cases. Ramberg-Osgood equation establishes a description of stress-strain curve by three parameters [35]. Taking as a reference its explicit form, a variant of the same is proposed. This is written as

$$\sigma = \frac{E_0 \varepsilon}{\left(1 + \left(\frac{E_0 \varepsilon}{\beta \sigma_{\max}}\right)^n\right)^{1/n}}, \tag{3}$$

where E_0 and $\sigma_{\max}$ are the initial modulus and the maximum strength, respectively, which were obtained from the numerical response, n is a parameter related to the speed of asymptotic convergence and β is a parameter that provides the asymptotic stress when multiplied by $\sigma_{\max}$. The curve fittings shown in Fig. 4 demonstrate the suitability of such an equation for modelling transverse as well as in-plane shear behaviours. The numerical response for each of the cases presented here is analysed in detail below.

[Figure 4 about here.]

The fracture process under pure transverse tensile stress was controlled by fibre/matrix interface debonding. This phenomenon was evidenced by the formation of debonds on the poles of the fibres according to the load direction. The hotspots were identified between the fibre clusters due to the stress concentration. At a certain load level, such areas reached a significant level of inelastic deformation, causing the integrity of the microstructure to be maintained only by the loading of matrix ligaments, which ultimately failed. At a global level, a crack perpendicular to the loading direction appeared (see Fig. 4(a)). The predicted average transverse elastic modulus, $E_2 = 13.53\,\text{GPa}$, was quite similar to that obtained by using the Halpin-Tsai approximation ($E_2 = 14.5\,\text{GPa}$) [36]. The predicted average transverse tensile strength, Y^{t}, and strain-to-failure were considered reasonable when compared to those obtained experimentally by Yudhanto *et al.* [37].

Under pure transverse compression, the failure was promoted by the generation of shear bands in the matrix (see Fig. 4(b)). To reach this stage, the fibre/matrix interface once again played a significant role. Since the ISS, τ^0, was lower than the PP matrix shear strength, initially an interface debonding phenomenon took place on the poles of some of the fibres and perpendicular to the load direction. Subsequently, the matrix was plastically deformed leading to shear bands and according to a preferential orientation of $\approx 50°$. The average compression transverse elastic modulus was, as expected, the same as that for the tensile case. The computed average compression transverse strength, Y^{c},

resulted in ≈ 68 MPa, this being reasonable according to data available in the literature [38].

As for the shear response, two loading cases were analysed: parallel to the fibres and perpendicular to the fibres. The reason was that, once a certain level of deformation had been reached ($\approx 7\%$), due to fibre rotation, a gradual increase in stress was expected in the perpendicular case compared to the parallel case [39]. However, this phenomenon does not occur in the present analyses, as the failure occurs in both cases studied for a relatively low level of deformation ($\approx 3\%$) (see Fig. 4(c-d)). Since the fibre/matrix interface was the weakest entity, the fracture process was triggered by interface debonding. As this phenomenon spreads, a plastic deformation band developed, culminating in the failure of the microstructure. The average shear modulus and shear strength were obtained as $G_{12} = 4.91$ GPa and $S^{\mathrm{l}} \approx 27$ MPa, respectively.

4.2. RVE–2: longitudinal tension

[Figure 5 about here.]

Fig. 5 shows the longitudinal tensile stress-strain curves predicted by RVE–3 for five different microstructures with their corresponding random fibre strength assignments according to Weibull distribution. The longitudinal tensile response revealed a linear behaviour practically up to the moment of failure (see Fig. 5). The curve lost linearity when the first fibre breakage occurred. It can be observed that this event can occur at about 60% of the total load bearing capacity. However, discerning at a glance its effect on the loading curve is not straightforward. With this first occurrence, a sequence of fibre breakage events were triggered until the collapse of the microstructure, as schematically shown in Fig. 5 for one of the cases analysed. It should be noted that in order to obtain a more accurate prediction of longitudinal tensile strength it would be necessary to carry out a RVE size sensitivity study. The size used in this study ($h_o \approx 120$ µm; see Fig. 3(b)) established that the critical cluster size is 6 fibres. This was assumed to be a valid size; however, it should be noted that there is a possibility that it may be larger. According to the above, the average longitudinal tensile elastic modulus, E_{11}, and longitudinal tensile strength, X^{t}, resulted as 50.85 GPa and 1947 MPa, respectively.

4.3. RVE–3: longitudinal compression

Fig. 6 shows the longitudinal compressive elastic modulus, $E_1^{\mathrm{c}}(\phi_0)$, and strength, $X^{\mathrm{c}}(\phi_0)$, predicted by the model as a function of initial misalignment angle, ϕ_0. The modulus was hardly influenced, but the resistance significantly decreased with ϕ_0. The latter was also compared with the analytical solution based on LaRC04 criterion [40] and the one proposed by Pimenta *et al.* [41] (see Fig. 6). Given the good correlation, the numerical prediction was considered reasonable, as it falls between the two analytical solutions, all of them being very similar for a misalignment angle above 2°.

Once $X^{\mathrm{c}}(\phi_0)$ is known, the determination of the longitudinal compressive strength depends on knowing the representative initial misalignment angle. The

use of a fibre misalignment probability density function determined by experimental methods such as those proposed by Czabaj *et al.* [42] and Yugartis [43] would be the most adequate, as followed by Naya *et al.* [33]. Unfortunately, there is no such data available for GFPP, and their determination would be tedious and expensive. Instead, and for the sake of simplicity, representative misalignment angles of E-glass fibre-reinforced composites were taken from literature and a range of interest, delimited by an upper limit ($\phi_0^{\max} = 3.23°$) and a lower limit ($\phi_0^{\min} = 2.74°$), was defined. These limits were established by averaging the misalignment angles of E-glass fibre-reinforced composites obtained by two statistically different methods analysed by Barbero and Tomblin (see Table 3. in [44]). Fig. 7 shows the prediction of RVE–3 for these limit values, as well as for the intermediate value $\phi_0 = 2.98°$.

The sequence of events during the compression process can be described as follows. Once a certain deformation ($\varepsilon_{11} \approx 0.5\%$) was reached, the fibre kinking mechanism was activated by the failure of the interface in the region of fibre which has the maximum misalignment (central region in RVE–3). Fig. 7 shows this evolution (for the case of $\phi_0 = 2.98°$) based on the percentage of debonded interface (with blue diamond-shape marks). The damage at the interface propagates along longitudinal and circumferential paths, progressively increasing the debonded area and reducing the load transferred between the fibre and the matrix. Finally, at $\varepsilon_{11} \approx 0.83\%$, the circumferentially-propagated damage in the plane of maximum misalignment had covered almost the entire perimeter of the fibre, leading to the instability and collapse of the model.

[Figure 6 about here.]

[Figure 7 about here.]

[Table 2 about here.]

5. Conclusions

The mechanical properties of a thermoplastic yarn from a glass fibre-reinforced polypropylene (GFPP) woven fabric were determined by using computational micromechanics. Firstly, the properties of the microconstituents were obtained by in-situ characterisation tests. Secondly, these properties were used to feed three different RVE models which allowed the prediction of the yarn longitudinal, transverse and shear responses of the thermoplastic yarn. Contrary to what is observed for thermoset composites, the homogenised yarn constitutive behaviour was found to be characterised by significant non-linearity until failure, specially in transverse and shear directions. Such characteristics would have been difficult to obtain by means of experimental methods. Hence, computational micromechanics is revealed to be of great value in the analysis of thermoplastic composite materials. With the information obtained, a constituent model of the yarn can be formulated, being therefore possible to move upward in the multiscale modelling strategy to predict the ply properties at the mesoscale, as will be demonstrated in a follow-up work.

Acknowledgements

The research leading to the developments described received funding of the project ADVANSEAT; a collaborative R&D project led by Grupo Antolín, and partially supported by the Spanish Ministry of Economy, Industry and Competitiveness (MINECO). C.S. Lopes also acknowledges the support of MINECO through the *Ramón y Cajal* fellowship (RYC-2013-14271).

Data availability

The raw/processed data required to reproduce these findings cannot be shared at this time as the data also forms part of an ongoing study.

References

[1] Llorca J, González C, Molina-Aldareguía JM, Segurado J, Seltzer R, Sket F, et al. Multiscale modeling of composite materials: A roadmap towards virtual testing. Advanced Materials 2011;23(44):5130–47.

[2] Lopes CS, González C, Falcó O, Naya F, LLorca J, Tijs B. Multiscale virtual testing: the roadmap to efficient design of composites for damage resistance and tolerance. CEAS Aeronautical Journal 2016;7(4):607–19.

[3] González C, Vilatela J, Molina-Aldareguía J, Lopes C, LLorca J. Structural composites for multifunctional applications: Current challenges and future trends. Progress in Materials Science 2017;89:194–251.

[4] González C, LLorca J. Mechanical behavior of unidirectional fiber-reinforced polymers under transverse compression: Microscopic mechanisms and modeling. Composites Science and Technology 2007;67(13):2795–806.

[5] Totry E, González C, LLorca J, Molina-Aldareguía JM. Mechanisms of shear deformation in fiber-reinforced polymers: experiments and simulations. International Journal of Fracture 2009;158(2):197–209.

[6] Vaughan T, McCarthy C. A micromechanical study on the effect of intraply properties on transverse shear fracture in fibre reinforced composites. Composites Part A: Applied Science and Manufacturing 2011;42(9):1217–28.

[7] Vaughan TJ, McCarthy CT. Micromechanical modelling of the transverse damage behaviour in fibre reinforced composites. Composites Science and Technology 2011;71(3):388–96.

[8] Canal LP, González C, Segurado J, LLorca J. Intraply fracture of fiber-reinforced composites: Microscopic mechanisms and modeling. Composites Science and Technology 2012;72(11):1223–32.

[9] Totry E, LLorca J, González C. Failure locus of fiber-reinforced composites under transverse compression and out-of-plane shear. Compos Sci Technol 2008;68(3-4):829–39.

[10] Totry E, González C, LLorca J. Influence of the loading path on the strength of fiber-reinforced composites subjected to transverse compression and shear. International Journal of Solids and Structures 2008;45(6):1663–75.

[11] Totry E, González C, LLorca J. Prediction of the failure locus of C/PEEK composites under transverse compression and longitudinal shear through computational micromechanics. Composites Science and Technology 2008;68(15-16):3128–36.

[12] Romanowicz M. A numerical approach for predicting the failure locus of fiber reinforced composites under combined transverse compression and axial tension. Computational Materials Science 2012;51(1):7–12.

[13] Melro A, Camanho P, Andrade Pires F, Pinho S. Micromechanical analysis of polymer composites reinforced by unidirectional fibres: Part II Micromechanical analyses. International Journal of Solids and Structures 2013;50(11-12):1906–15.

[14] Pulungan D, Lubineau G, Yudhanto A, Yaldiz R, Schijve W. Identifying design parameters controlling damage behaviors of continuous fiber-reinforced thermoplastic composites using micromechanics as a virtual testing tool. International Journal of Solids and Structures 2017;117:177–90.

[15] Xu Q, Qu S. Multiscale simulation of damage progression in 5-Harness satin weave Composites. JOM 2015;67(7):1491–8.

[16] Lanxess . Tepex® dynalite 104-RG600(x)/47% - Material data sheet. 2017.

[17] Rodríguez M, Molina-Aldareguía J, González C, LLorca J. A methodology to measure the interface shear strength by means of the fiber push-in test. Composites Science and Technology 2012;72(15):1924–32.

[18] Rodríguez M, Molina-Aldareguía J, González C, LLorca J. Determination of the mechanical properties of amorphous materials through instrumented nanoindentation. Acta Mater 2012;60(9):3953–64.

[19] Zhai Z, Gröschel C, Drummer D. Tensile behavior of quasi-unidirectional glass fiber/polypropylene composites at room and elevated temperatures. Polymer Testing 2016;54:126–33.

[20] Oliver W, Pharr G. An improved technique for determining hardness and elastic modulus using load and displacement sensing indentation experiments. Journal of Materials Research 1992;7(6):1564–83.

[21] Ogihara S, Koyanagi J. Investigation of combined stress state failure criterion for glass fiber/epoxy interface by the cruciform specimen method. Composites Science and Technology 2010;70(1):143–50.

[22] Molina-Aldareguía JM, Rodríguez M, González C, LLorca J. An experimental and numerical study of the influence of local effects on the application of the fibre push-in test. Philosophical Magazine 2010;91(7-9):1293–307.

[23] Dassault Systèmes . Abaqus Documentation 2018. 2018.

[24] Segurado J, Llorca J. A numerical approximation to the elastic properties of sphere-reinforced composites. Journal of the Mechanics and Physics of Solids 2002;50(10):2107–21.

[25] Drucker D, Prager W. Soil Mechanics and Plastic Analysis or Limit Design. Quarterly of Applied Mathematics 1952;9(2):157–65.

[26] Payandehpeyman J, Majzoobi GH, Bagheri R. Determination of the extended Drucker-Prager parameters using the surrogate-based optimization method for polypropylene nanocomposites. Journal of Strain Analysis for Engineering Design 2016;51(3):220–32.

[27] Camanho PP, Dávila CG. Mixed-Mode Decohesion Finite Elements in for the Simulation Composite of Delamination Materials. Tech. Rep. June; National Aeronautics and Space Administration (NASA); 2002.

[28] Benzeggagh ML, Kenane M. Measurement of Mixed-Mode Delamination Fracture Toughness of Unidirectional Glass / Epoxy Composites With Mixed-Mode Bending Apparatus. Composites Science and Technology 1996;56(4):439–49.

[29] Naya F. Prediction of mechanical properties of unidirectional FRP plies at different environmental conditions by means of computational micromechanics. Ph.D. thesis; Universidad Politécnica de Madrid; 2017.

[30] González C, LLorca J. Multiscale modeling of fracture in fiber-reinforced composites. Acta Materialia 2006;54(16):4171–81.

[31] Curtin WA. Theory of Mechanical Properties of Ceramic-Matrix Composites. Journal of the American Ceramic Society 1991;74(11):2837–45.

[32] Weibull W. A statistical theory of the strength of materials. Tech. Rep.; 1939.

[33] Naya F, Herráez M, Lopes C, González C, Van der Veen S, Pons F. Computational micromechanics of fiber kinking in unidirectional FRP under different environmental conditions. Composites Science and Technology 2017;144:26–35.

[34] Herráez M, Bergan AC, González C, Lopes CS. Multiscale fiber kinking : computational micromechanics and a mesoscale continuum damage. Tech. Rep.; 2017.

[35] Ramberg W, Osgood WR. Description of stress-strain curves by three parameters – Technical Note No. 902. Tech. Rep.; National Advisory Committee for Aeronautics (NACA); 1943.

[36] Halpin J. Effects of Environmental Factors on Composite Materials. Technical Report Afml-Tr-67-423 1967;.

[37] Yudhanto A, Lubineau G, Wafai H, Mulle M, Pulungan D, Yaldiz R, et al. Monotonic and cyclic responses of impact polypropylene and continuous glass fiber-reinforced impact polypropylene composites at different strain rates. Polymer Testing 2016;51:93–100.

[38] Rausch J, Zhuang RC, Mäder E. Systematically varied interfaces of continuously reinforced glass fibre/polypropylene composites: Comparative evaluation of relevant interfacial aspects. Express Polymer Letters 2010;4(9):576–88.

[39] Totry E, Molina-Aldareguía JM, González C, LLorca J. Effect of fiber, matrix and interface properties on the in-plane shear deformation of carbon-fiber reinforced composites. Composites Science and Technology 2010;70(6):970–80.

[40] Pinho ST, Dávila CG, Camanho PP, Iannucci L, Robinson P. Failure Models and Criteria for FRP Under In-Plane or Three-Dimensional Stress States Including Shear Non-linearity. Tech. Rep.; National Aeronautics and Space Administration (NASA); 2005.

[41] Pimenta S, Gutkin R, Pinho S, Robinson P. A micromechanical model for kink-band formation: Part IIAnalytical modelling. Composites Science and Technology 2009;69(7-8):956–64.

[42] Czabaj MW, Riccio ML, Whitacre WW. Numerical reconstruction of graphite/epoxy composite microstructure based on sub-micron resolution X-ray computed tomography. Composites Science and Technology 2014;105:174–82.

[43] Yurgartis S. Measurement of small angle fiber misalignments in continuous fiber composites. Composites Science and Technology 1987;30(4):279–93.

[44] Barbero EJ, Tomblin J. A damage mechanics model for compression strength of composites. International Journal of Solids and Structures 1996;33(29):4379–93.

List of Figures

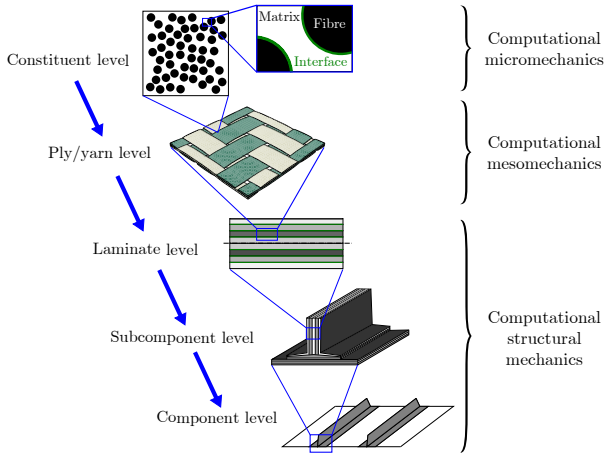

Figure 1: Hierarchical scheme showing the different identifiable entities within a composite structure, classifying them according to the three main length scales.

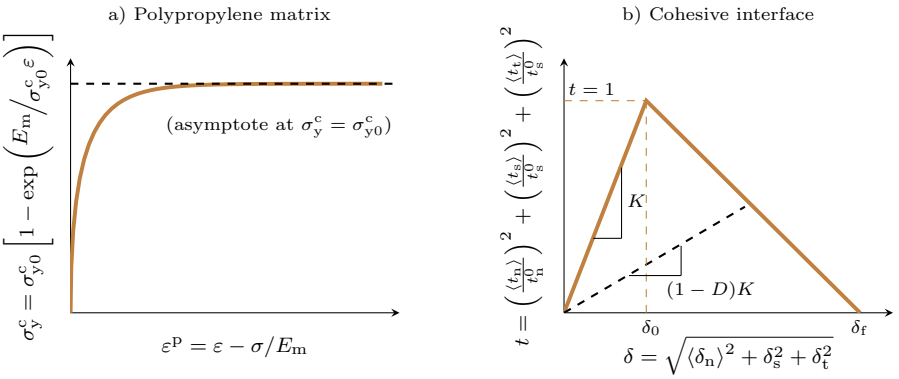

Figure 2: (a) Hardening evolution law of the PP matrix as a function of the elastic modulus, E_m, and the asymptotic value of the yield strength, σ_{y0}^c. (b) Cohesive interaction response with respect to the effective separation, δ_m, defined by Camanho and Dávila [27].

a) RVE–1: transverse and in-plane shear loading simulations

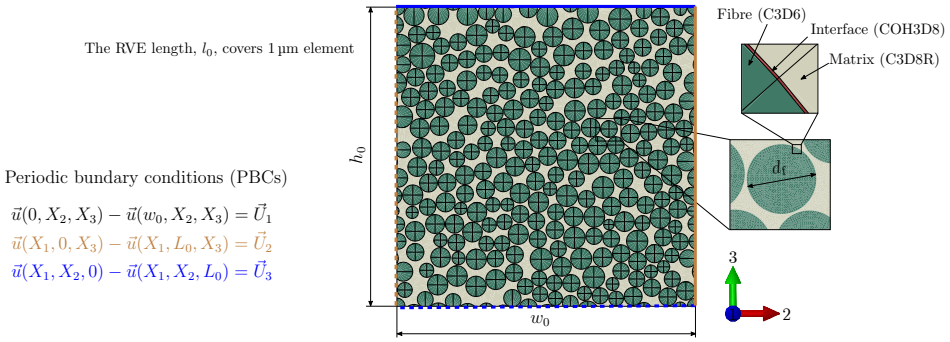

b) RVE–2: longitudinal tension loading simulations

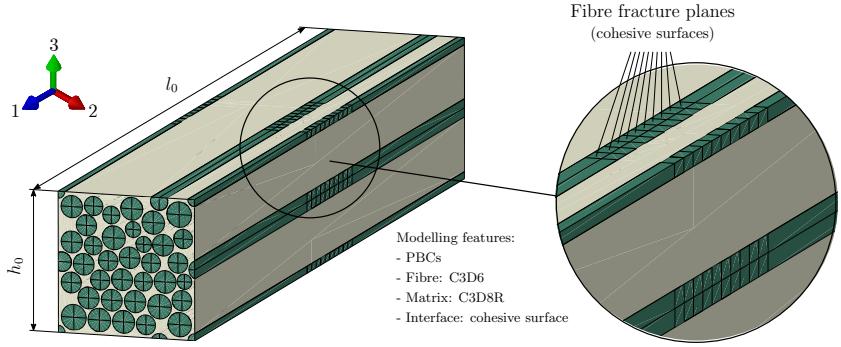

c) RVE–3: longitudinal compression loading simulations

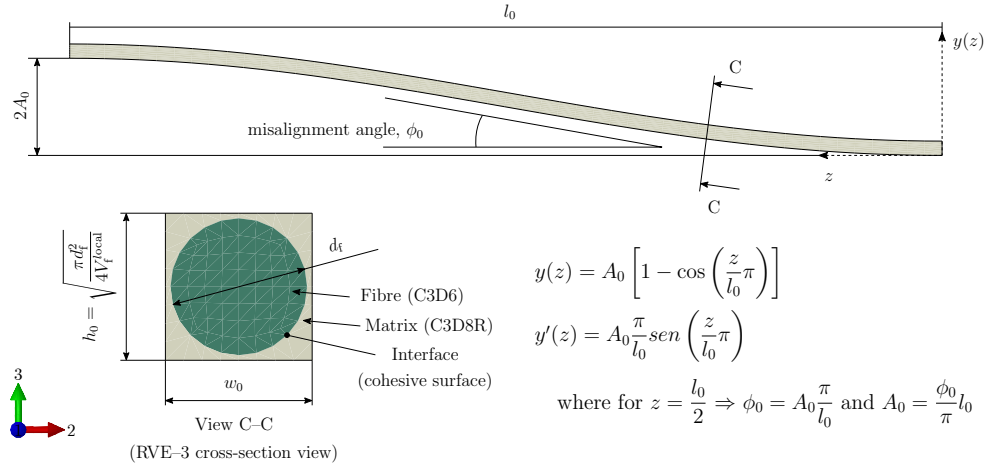

Figure 3: Schematic representation of the three RVE models: (a) RVE–1, (b) RVE–2 and (c) RVE–3; with their main modelling features.

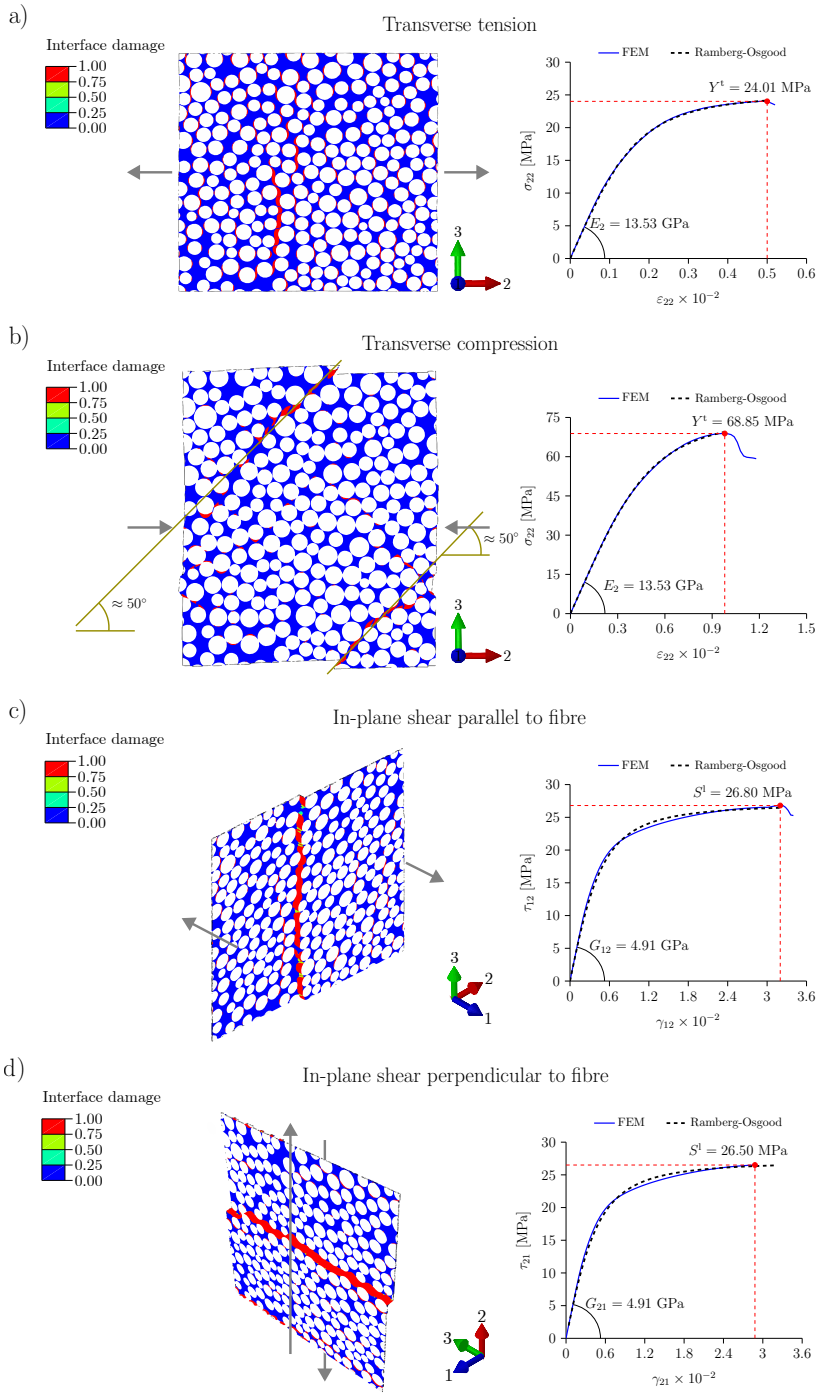

Figure 4: Prediction of RVE–1 for the (a) transverse tension, (b) transverse compression, (c) in-plane shear parallel to fibre and (d) in-plane shear perpendicular to fibre.

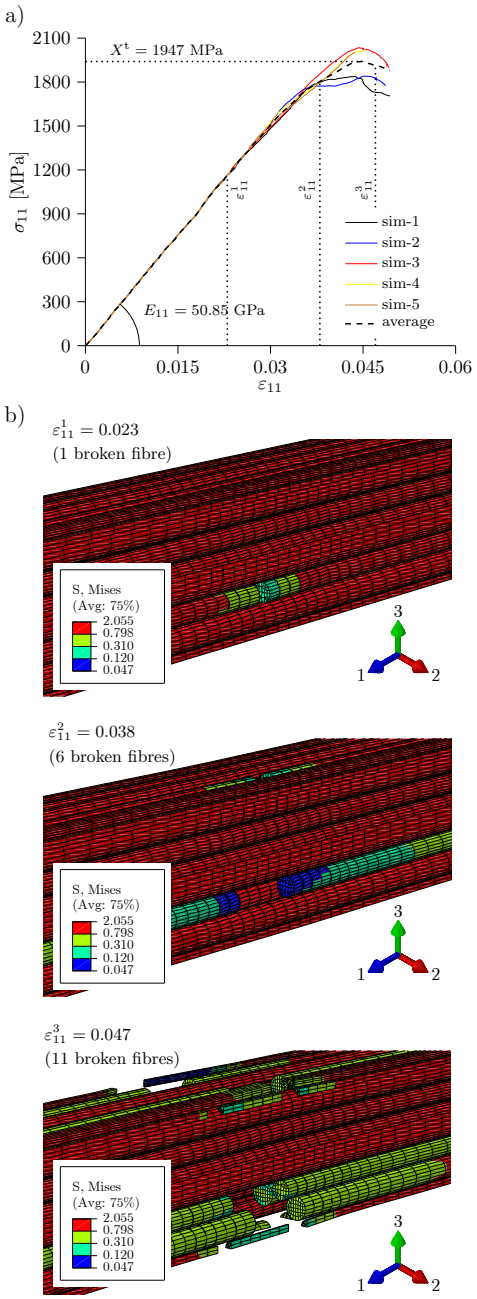

Figure 5: (a) Longitudinal tensile stress-strain curve predicted by RVE–3 for five different microstructures with their corresponding random fibre strength assignments according to Weibull distribution. (b) Evolution of tension and progressive failure of the fibres with strain for one of the cases.

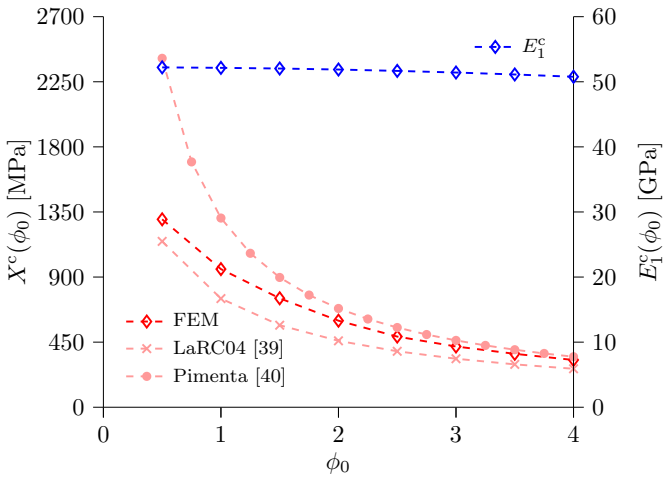

Figure 6: Longitudinal compression elastic modulus, $E_1^c(\phi_0)$, and strength, $X^c(\phi_0)$, predicted by RVE–3 as a function of initial misalignment angle, ϕ_0, in degrees. A comparison with analytical models from the literature is also included.

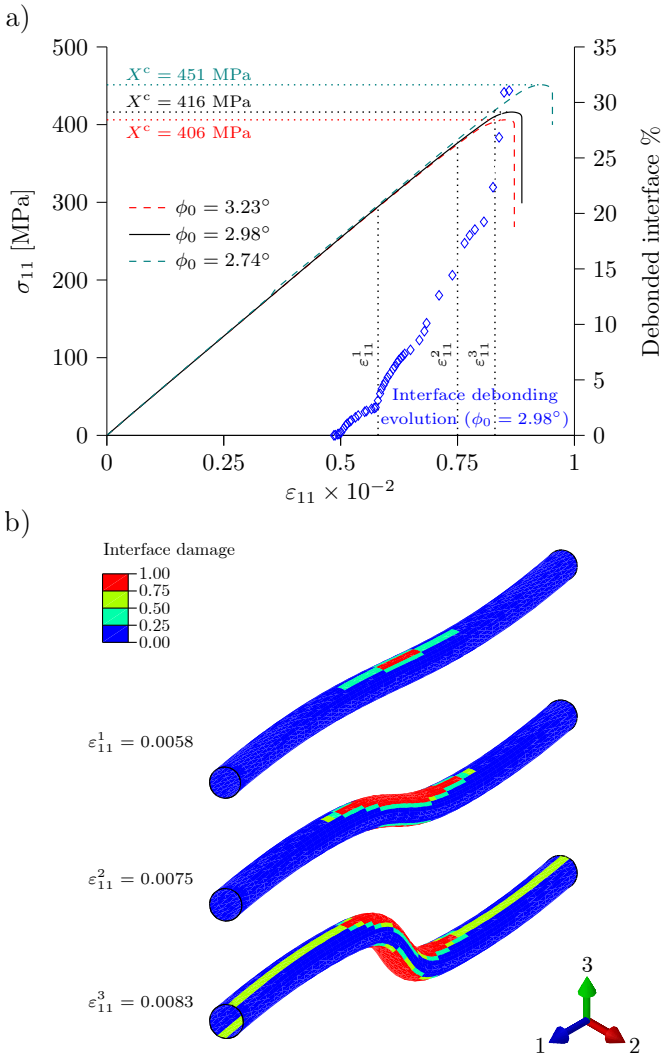

Figure 7: (a) Longitudinal compression stress-strain curve of the yarn predicted by RVE–3 for three misalignment angle values within the range of interest: $\phi_0 = 3.23°$ (upper limit), $\phi_0 = 2.74°$ (lower limit) and $\phi_0 = 2.98°$ (intermediate value). The evolution of the interface debonding (for the latter) is represented based on the percentage of debonded interface. (b) cohesive damage for different deformation stages ($\phi_0 = 2.98°$).

List of Tables

From RVE–1	
Trans. tension/compression elastic modulus	E_2
In-plane shear modulus	G_{12}
Trans. tensile strength	Y^{t}
Trans. compression strength	Y^{c}
In-plane shear strength	S^{l}
From RVE–2	
Long. tensile elastic modulus	E_1^{t}
Long. tensile strength	X^{t}
From RVE–3	
Long. compression elastic modulus	E_1^{c}
Long. compression strength	X^{c}

Table 1: Fundamental yarn properties to be determined from the RVE models.

Longitudinal tension	(*From* RVE–2)
$E_1^{\mathrm{t}} = 50.85\,\mathrm{GPa}$	
$X^{\mathrm{t}} = 1947\,\mathrm{MPa}$	
Longitudinal compression	(*From* RVE–3)
$E_1^{\mathrm{c}} = 50.94\,\mathrm{GPa}$	
$X^{\mathrm{c}} = 416\,\mathrm{MPa}$	
Transverse tension	(*From* RVE–1)
$E_2^{\mathrm{t}} = 13.53\,\mathrm{GPa}$	
$Y^{\mathrm{t}} = 24.01\,\mathrm{MPa}$	
$\beta = 1.05$	
$n = 2.33$	
Transverse compression	(*From* RVE–1)
$E_2^{\mathrm{c}} = 13.53\,\mathrm{GPa}$	
$Y^{\mathrm{c}} = 68.85\,\mathrm{MPa}$	
$\beta = 1.09$	
$n = 2.59$	
In-plane shear	(*From* RVE–1)
$G_{12} = 4.91\,\mathrm{GPa}$	
$S^{\mathrm{l}} = 26.80\,\mathrm{MPa}$	
$\beta = 1$	
$n = 1.84$	

Table 2: Fundamental yarn properties obtained from the RVE models.